2021

Integrating Multiscale Numerical Simulations with Machine Learning to Predict the Strain Sensing Efficiency of Nano-Engineered Smart Cementitious Composites

Gideon A. Lyngdoh

Sumanta Das

Integrating multiscale numerical simulations with machine learning to predict the strain sensing efficiency of nano-engineered smart cementitious composites

Gideon A. Lyngdoh, Sumanta Das *

Department of Civil and Environmental Engineering, University of Rhode Island, Kingston, RI, USA

HIGHLIGHTS

- Strain-sensing ability of a nanoengineered self-sensing cementitious composite is assessed by integrating multiscale finite element analysis simulations and machine learning.
- Hyperparameter-optimized feed-forward multilayer perceptron-based neural network showed excellent efficacy for the prediction of strain-sensing ability.
- Shapley Additive Explanations algorithm reveals that coating thickness shows higher influence on the sensing ability than fraction of coated sand.
- Comprehensive approach presented here can be used as starting point toward development of reliable performance standards for self-sensing cementitious composites.

GRAPHICAL ABSTRACT

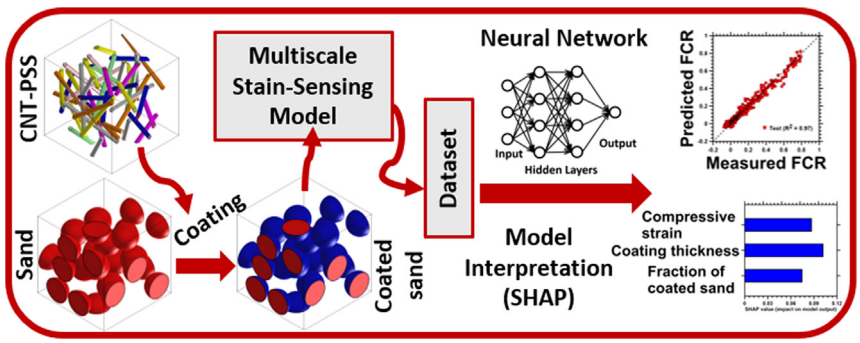

ABSTRACT

Prediction of in-situ strain sensing efficiency of self-sensing cementitious composites using machine learning (ML) requires a large, representative, consistent, and accurate dataset. However, such large experimental dataset is not readily available. Moreover, the success of the ML approach depends on its ability to abide by the fundamental laws of physics. To address these challenges this paper synergistically integrates a validated finite element analysis (FEA)-based multiscale simulation framework with ML to predict the strain-sensing ability of self-sensing cementitious composites enabled by incorporating nano-engineered interfaces. The multiscale simulation framework is leveraged to develop a balanced, representative, complete, and consistent dataset containing 3000 combinations of strain-dependent electromechanical responses. This large dataset is used to predict the strain-sensing ability of the nanoengineered cementitious composites using a feed-forward multilayer perceptron-based neural network (NN) approach which shows excellent prediction efficacy. This paper also applies a Shapley Additive Explanations (SHAP) algorithm to interpret the NN predictions in light of the relative importance of different design parameters on the strain-sensing ability of the composite. Overall, the synergistic and comprehensive approach presented here can be used as a starting point toward the development of reliable

Keywords:
Machine learning
Neural network
Piezo-resistivity
Strain-sensing
Micromechanics
Multiscale numerical simulation

performance standards to accelerate the acceptance of these self-sensing cementitious composites for large-scale applications.

1. Introduction

Structural Health Monitoring (SHM) [1–5] enables timely inspection and maintenance of structures. The core functions of the SHM are to detect and locate the damages of the large-scale structures, evaluate and quantify the severity of the damage, predicting the service life of the structures, and real-time monitoring and diagnosis of the structural condition [6]. In the past, the most common non-destructive test (NDT) techniques adopted were ultrasound testing [7], thermography [8], radiography [9], X-rays [10], etc. These approaches require direct access to parts of the structures which are not always easily accessible [11]. Thus, their application towards detailed structural health monitoring (SHM) in large-scale structures becomes limited. Although the development of external sensors for SHM has been thoroughly discussed in the literature [11,12], for real applications, the obvious drawbacks of these techniques are high cost; time-consuming, labor-intensive installation and maintenance; lower performance efficiency in extreme environments which limit their performance and deployment on civil structures [13–15]. Moreover, such a technique is practically exhaustive for large structures because of the requirement of a large number of sensors to cover such large surfaces which may not be realistically viable. Besides these existing problems, for complex structures, most of the damage-prone parts are inaccessible. The breakthrough in SHM came after integrating different modern technologies such as magnetic, electrical, thermal response evaluation with computer science technologies [16]. Hence, sensing technology has gained more attention in the past decade to circumvent the existing issues [11,12]. Modern SHM techniques require a sensory system, a data acquisition system, transmission, a management system, and an evaluation or diagnosis of structural health. The most crucial part of the SHM system is the reliable and stable sensing system. Several sensing techniques have been proposed and implemented with specific functions and mechanisms to diagnose and evaluate the structural condition properly [2,6,17]. Damage assessment in the concrete using the SHM tool can be realized with the help of strain measurements such as strain gauges [18] or vision-based measurements [19]. These techniques are integrated with remote sensing and smart materials combined with a computer-based knowledge system in which the performance of large infrastructures such as tunnels, bridges, offshore platforms, railways, and other inaccessible sites can be monitored and evaluated [20]. The major problem with these monitoring devices is the compatibility between the sensor and the concrete structure [21] and environmental interference [11]. Therefore, there is a need to develop advanced SHM sensing technologies. Detailed reviews on the sensors for health monitoring of concrete structures can be found in the literature [11,12].

With the rapid growth in modern science and engineering, it is possible to develop a smart/intelligent cementitious material that has its own sensing functionality without the integration of any external sensing element [15]. Smart-cementitious materials, also known as intrinsic self-sensing, are fabricated by incorporating functional fillers such as carbon fibers (CF) [22–24], carbon nanotubes (CNTs) [25–27], graphene [28], and nickel powder [29] into traditional concrete. These intrinsic functional materials are inherently electrically conductive in nature. Any changes in the cementitious composite caused by applying forces or environmental actions can alter the network connectivity, leading to changes in the composite electrical properties such as electrical resistance. Such a nature is attributed to piezoresistive behavior. Thus, by incorporating smart-nanoengineered materials, cementitious materials can surpass the issue of incompatibility in civil structures and enable a self-sensing mechanism to the whole structure. Owing to piezoresistivity, these smart composites have been used for strain and damage-sensing [22,30–36]. One of the major drawbacks in this domain has been the issue of agglomeration of conductive additives such as CNTs and, if the functional additives are not appropriately dispersed, this can lead to poor performance by preventing the formation of the network connectivity which is necessary to enable strain sensing. Simply increasing the fiber concentration can overcome this issue, but it is impractical since it can adversely affect the workability of the mixtures, and also it leads to higher costs [37–39]. An alternative solution has been proposed where CNT-based thin films are used as coatings around the sand particles to modify the cement paste-aggregate interfaces [37–42]. This approach has been shown to preserve the mechanical properties of the system and, at the same time, it enables enhanced strain and damage sensing. Such an approach has shown to be cost-effective and sensitive to deformation, making them attractive to SHM in concrete structures [37–39]. Such smart mortars can be potentially applied as coating or overlays on the existing large concrete structures to enable strain sensing and structural health monitoring. Despite the progressive research in smart cementitious material, this procedure has not been extensively implemented in industrial applications. One of the major reasons behind this could be attributed to the lack of reliable performance standards.

While experimental studies have been widely reported evaluating the electromechanical response for such self-sensing cementitious composites enabled by implementing nano-engineered inclusion-matrix interfaces [37–40,43], limited numerical studies exist on the prediction of strain sensing efficiency of such systems [44]. Although limited numerical studies are available towards the prediction of strain-sensing efficiency of smart cementitious composites with nano-engineered interfaces, a wide range of numerical studies for smart polymer composites are available in the literature. Electro-mechanical modeling has been implemented to predict the response of CNT-polymer composites using equivalent resistor network models, micromechanics-based models, and by developing analytical models. The equivalent resistor models [45–50] are developed by considering the interactions of individual nanofillers in which they collectively form inter-connected networks within a microscale domain. However, these models are computationally expensive as a large number of nanofillers are needed to form a percolated network. On the other hand, the analytical techniques [51–53] are not computationally demanding. However, oversimplification of heterogeneity in these analytical models often results in inadmissible predictions especially when there is damage in the system or when large deformations are considered. Electro-mechanical models are also developed to predict the response of CNT-polymer composites implementing higher-order tensor-based resistivity-strain relations which showed excellent predictions under complex strain states [53]. Computational micromechanics-based models [54–61], on the other hand, are able to mimic the intricate microstructural features present in such heterogenous composites only being limited by high computational expense. The multiscale computational homogenization

essentially associates a heterogenous unit cell to every Gauss point of the virtual macro-homogenous structure in the subsequent scales. The robustness of the approach lies in its ability to capture both physical and geometric evolution at each scale resulting in a homogenized constitutive relation at the top length scale. In other words, no a-priori constitutive information is assumed for the macro-level problem which is instead obtained from the volume-averaged field response of the unit cell (representative of the previous length scale) when subjected to a unit gradient. This is achieved by solving a boundary value problem on a unit cell with consistent boundary conditions obeying the Hill-Mandel principle that equates work done at interactive length scales. Multiscale numerical simulation of CNT-based polymer composites has gained significant attention in the past few decades. The mechanical properties of these hierarchical composite materials are evaluated by either following the bottom-up approach [62] or the top-down approach [63]. Such approaches can be implemented either by hierarchically homogenizing the properties at every interactive length scale [61–65] or by using a concurrent framework [66]. Upscaling the properties of composites from nanoscale to higher scale has garnered significant attention over the years where the characteristics of the matrix and the fiber–matrix interfaces are simulated using molecular dynamics (MD) simulations [61,64]. By evaluating the stress transfer behavior at multiple length scales, such multiscale simulations provide valuable insights towards enhancing the mechanical properties of these composites. Recently, machine learning-based interatomic potentials have been implemented to enable first-principles multiscale modeling of lattice thermal conductivity in graphene/borophene heterostructures [67].

For self-sensing cementitious composites with nano-engineered inclusion-matrix interfaces, a microstructure-guided electromechanical response prediction framework was developed by the authors [44] for a large class of smart heterogeneous materials. Despite the progressive research on smart cementitious materials enabled by nano-engineered inclusion-matrix interfaces, this procedure has not been extensively implemented in industrial applications. One of the major reasons behind this could be attributed to the lack of reliable performance standards. While multiscale simulation-based predictive models have been developed [61,64,68–72] for self-sensing cementitious composites, these models are computationally expensive because of hierarchical intricacies at multiple length scales. Because of such high computational demand and complex modeling approaches, such computational approaches have not captivated the civil engineering materials industries.

Towards this, the primary focus of this paper is to synergistically integrate high throughput multiscale numerical simulations with machine learning (ML) to develop a robust and yet user-friendly simple predictive model for efficient prediction of electromechanical response of such smart cementitious composites. In particular, a feed-forward neural network [73] is implemented here. Such ML-based predictive models can be used as a starting point toward enabling the development of simple and user-friendly materials design tools that can be easily leveraged by designers and decision-makers for the widespread application of these emerging in-situ strain-sensing cementitious materials.

2. Methodology

2.1. Multiscale simulation approach

To evaluate the piezoresistive nature of the self-sensing cementitious composites, two different hierarchical length scales are implemented here, as shown in Fig. 1.

The first scale defines the characteristics of the coating, which contains carbon nanotubes (CNTs) and matrix. The second scale represents the mortar. At the mortar scale, mortar can be considered as a multi-phase composite material consisting of hardened cement paste matrix, sand inclusions, the coating around sand inclusions, and interfacial transition zone (ITZ) between the coated sand particles and the matrix. These ITZs form porous interfacial regions around the inclusions during the hydration of cement. Cement grains tend to pack loosely near and around the inclusion surfaces [74] which leads to the formation of these porous interfacial regions. ITZ is inherently the weakest link in concrete, and the damage in concrete is initiated at these weakest regions. Thus, ITZs play a critical role in defining the mechanical behavior of cementitious composites. Thus, this study adopts a hierarchical bottom-up approach [75,76] where the responses obtained from the CNT-PSS scale are assigned as coating properties around sand inclusions in the mortar scale to obtain the strain-sensing response of the mortars. Such an interactive approach requires an accurate representation of geometric parameters at each scale and a robust simulation framework as described hereafter.

The numerical simulation framework for the prediction of macroscopic electromechanical response of random heterogeneous smart materials is summarized in Fig. 2. It starts with the generation of unit cell geometry which is exported to the mechanical module to obtain stress response and deformed configuration when subjected to applied strain. As the performance of cementitious composites is primarily characterized by the compressive response, this paper evaluates the strain-sensing ability of the smart mortars in terms of uniaxial compressive response. However, it would be interesting to implement the aspect of multi-axial strain-sensing with non-dimensional responses, as reported in the literature [75,76] for CNT-based polymer composites, towards cementitious composites which can form an effective future study. The deformed geometry, as obtained from uniaxial compression simulation, is re-meshed in the remeshing module and exported to the electrical module. The electrical module applies external potential and obtains electric current density distribution in the unit cell. Thus, an electrical response is obtained for the unit cell for an applied strain. This process is repeated with strain increments to generate the electromechanical behavior of the composite. All these above-mentioned steps and modules are implemented at each length scale and are detailed in the forthcoming sub-sections.

2.1.1. Geometry generation approach

In this paper, the representative unit cells are generated by employing the Lubachhevsky-Stillinger algorithm [77,78]. In this algorithm, a hard contact model is implemented such that no overlapping of the inclusions is allowed. The random microstructure with inclusions is formed by randomly seeding the inclusion within a cubic matrix volume. The approach involves an iterative process where the inclusions are randomly assigned in the periodic bounding box and then subjected to a growth rate to obtain the desired particle size distribution. During the process, a constant velocity is assigned to update the position of the inclusions for every time increment and then are checked for any overlaps. The time increment at every step is considered as the minimum of those corresponding to every possible colliding inclusion pair. The algorithm continues to assign the positions of the inclusion resulting from collision and growth of inclusions within the bounding box at every step until the desired volume fraction is satisfied. The detailed formulations for generating the unit cell can be found in [44,79]. For the matrix, a homogenous solid section is generated where the solid matrix cut is obtained by taking the difference of geometric areas of the solid matrix and the inclusions. The inclusion embedded matrix geometry is obtained by stitching the

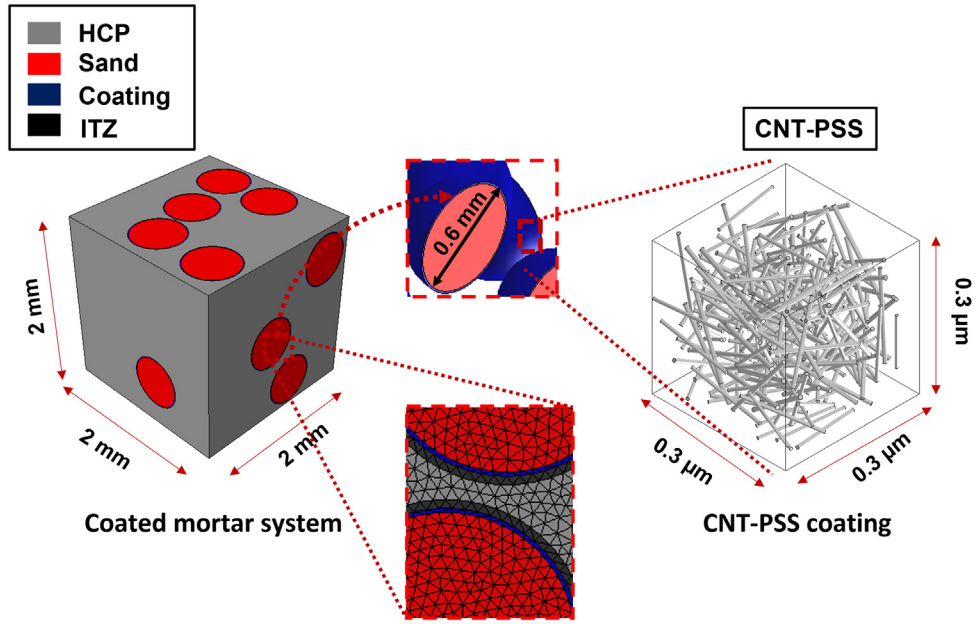

Fig. 1. Representative length scales implemented for electromechanical response evaluation.

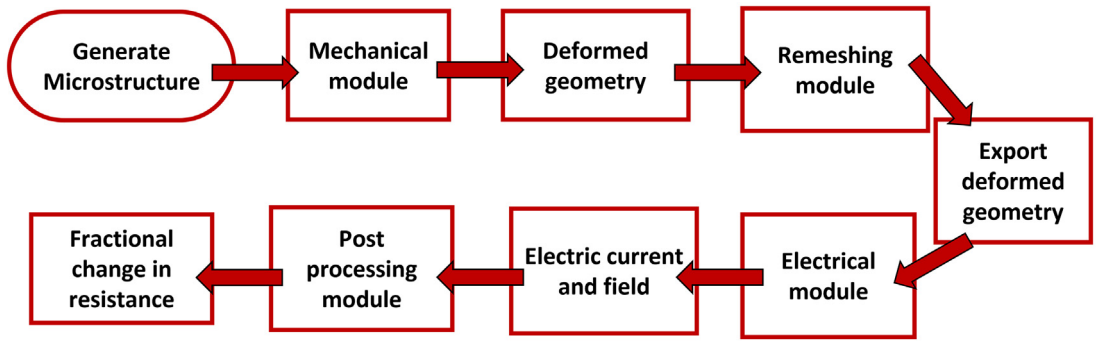

Fig. 2. Flowchart of the piezoresistive simulation framework.

solid cut geometry and the inclusions at the boundaries. Such unit cell generation algorithm has been also successfully applied in our previous studies [44,80]. Please refer to section B of the supplementary material for more details. The generated microstructure is then imported to commercial finite element software ABAQUS™ via python scripting and MATLAB subroutine.

2.1.2. Mechanical module

For mechanical response, the effective properties are evaluated for the RVEs after imposing periodic boundary conditions (PBCs). The constitutive relationship for a linear elastic material is written as

$$\sigma = \mathbb{C}\varepsilon \tag{1}$$

where σ, ε refer to the stress and strain vectors, and $\mathbb{C}$ corresponds to stiffness tensor. The averaged stress σ and strain ε vectors are described as spatial averages of the local distribution over the representative volume described as:

$$\sigma = \frac{1}{V}\int_V \sigma dV \tag{2}$$

$$\varepsilon = \frac{1}{V}\int_V \varepsilon dV \tag{3}$$

Since the effective properties are computed based on the repeated RVEs, the deformation of the RVE should be spatially periodic. This is achieved by applying PBCs along its boundary. The periodic boundary condition is imposed at the two opposite surface boundaries of the RVE at points A and B, where the respective displacement can be related as

$$u_k^A - u_k^B = \varepsilon_{avg}\left(x_k^A - x_k^B\right) = \varepsilon_{avg} L_{RVE} \tag{4}$$

where x is the position vector of the points A and B on the parallel boundaries, and L_{RVE} is the edge length of RVE. Eq. (4) is enforced in the simulation by setting constraint equations that relate the degree of freedom (DOF) of each pair of nodes on opposite boundaries to the 6 DOFs of a master node, corresponding to the 6 components of the homogenized strain tensor ε_{avg}. More details on the periodic boundary conditions are available in section D of the supplementary material. The representative steps involved in the mechanical module are shown in Fig. 3. The deformed geometry of the unit cell obtained from the mechanical module is re-meshed as described in the next sub-section.

2.1.3. Intermediate re-meshing rule

The re-meshing technique involves a mesh refinement on the deformed geometry wherever the aspect ratio of the elements

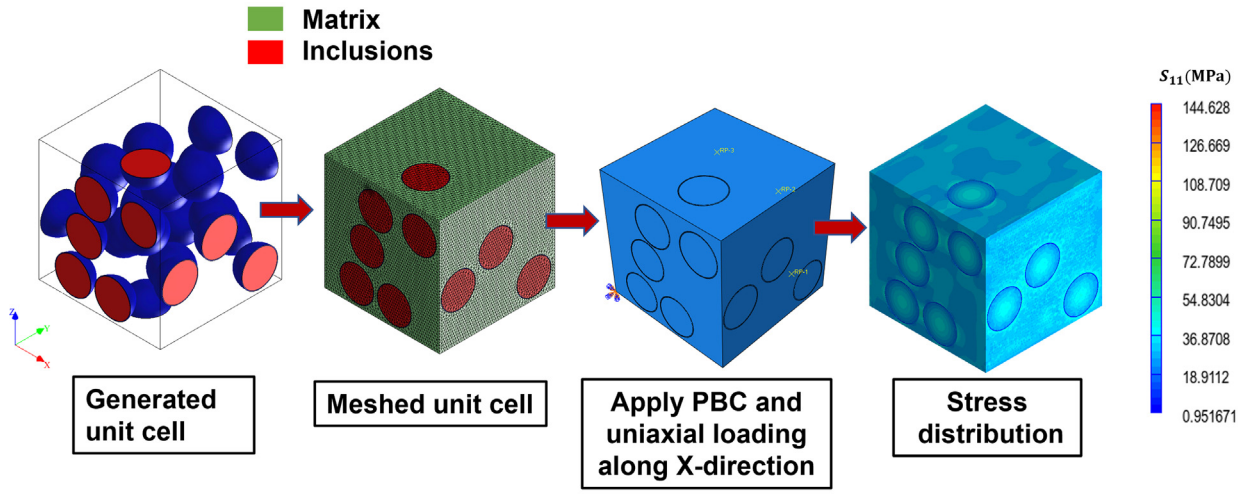

Fig. 3. Schematic representation of the mechanical module.

exceeds 3. This re-meshing module thus improves the quality of the mesh in the deformed unit cell. The re-meshed deformed geometry is then exported to the electrical module for electrical analysis. Similar implementation has also been successfully adopted elsewhere[44,69].

2.1.4. Electrical module

Similar to the mechanical analysis, the electrical response is evaluated for the RVEs at respective length scales. In finite element analysis, the electrical flow of current (J) can be described by Ohm's law where the constitutive equation is formulated as

$$J = \kappa E \tag{5}$$

where κ is the electrical conductivity tensor, and E is the electric field. The average quantities of the current density and electric field can be evaluated as

$$J = \frac{1}{V}\int_V JdV \tag{6}$$

$$E = \frac{1}{V}\int_V EdV \tag{7}$$

Hence, Eq. (5) can be reformulated in a homogenized sense as

$$\bar{\kappa} = \frac{J}{E} = \frac{\int_V JdV}{\int_V EdV} \tag{8}$$

The periodic boundary conditions for the electrical potential at the nodes of opposite boundaries are defined as

$$V^A - V^B = E\,L_{RVE} \tag{9}$$

The schematic representation of the electrical module is provided here in Fig. 4 for ease of reference.

2.1.5. Evaluation of the effective strain-sensing properties

After the mechanical module, remeshing module, and electrical module, the obtained responses are post-processed to yield an effective strain-sensing response. In this study, a unit potential difference is applied across the microstructure in one of the principal directions (say X). Using Ohm's Law (J = κ E), the electrical module computes current density (J) from the input electrical conductivity (κ) of component phases and the applied electric field (E). The simulation yields the electric field and current density distribution in the unit cell which when volumetrically averaged by a post-processing module results in an average conductivity. The average electrical conductivities are then expressed in terms of resistance. With varying strain, the change in resistance (ΔR) is calculated. Here the strain-sensing response is expressed by evaluating the fractional change in resistance (FCR) with varying strain. The FCR is calculated as the ratio of the change in resistance (ΔR) to the bulk resistance (R_0) as shown below [81]:

$$FCR = \frac{\Delta R}{R_0} \tag{10}$$

In order to observe the change in electrical response, the mapping is incorporated where the interpolated spatial distribution for defining solution-dependent material properties is implemented at every material domain [44,69].

2.1.6. Simulation approach for CNT- PSS matrix nanocomposite

In this study, the CNTs are generated as straight solid cylinders with a 2 nm radius, and the length is set to follow a gaussian distribution with a mean length of 100 nm and a standard deviation of 20 nm, as adopted from the literature [69]. The geometry generation approach mentioned in Section 2.1.1 is followed. The RVE considered herein has an edge length of 300 nm. The RVE size is adopted based on a sensitivity study [69]. A geometric periodicity is also implemented, which has been previously shown to evaluate the percolation effectively [69]. A target volume fraction of 0.035 is obtained based on the percolation studies as shown in the supplementary material. A similar volume fraction is achieved in a previous study for CNT-modified microstructures and such volume fraction has been shown to form percolating microstructure [69]. The RVE is then meshed, and periodic boundary conditions (PBCs) are implemented by constraining the nodes on the parallel surfaces. The formulation for PBC has been adequately detailed in the authors' previous publications [44,69,80]. A tetrahedral mesh (C3D10 elements) is used with a total of approximately 1,240,000 elements beyond which any further mesh refinement resulted in insignificant changes in the response. For simplicity, a perfect bonding is considered between the matrix and the inclusions. Under low compressive strains, the strain levels experienced within the CNT-PSS coating are well below the cracking strains, and as such damage state is not encountered within the CNT-PSS composite. Thus, under such low strain values, CNTs are considered perfectly bonded to the PSS matrix and damage models are not incorporated in the CNT-PSS scale. The geometry generation, meshing, and application of PBCs are implemented by using a

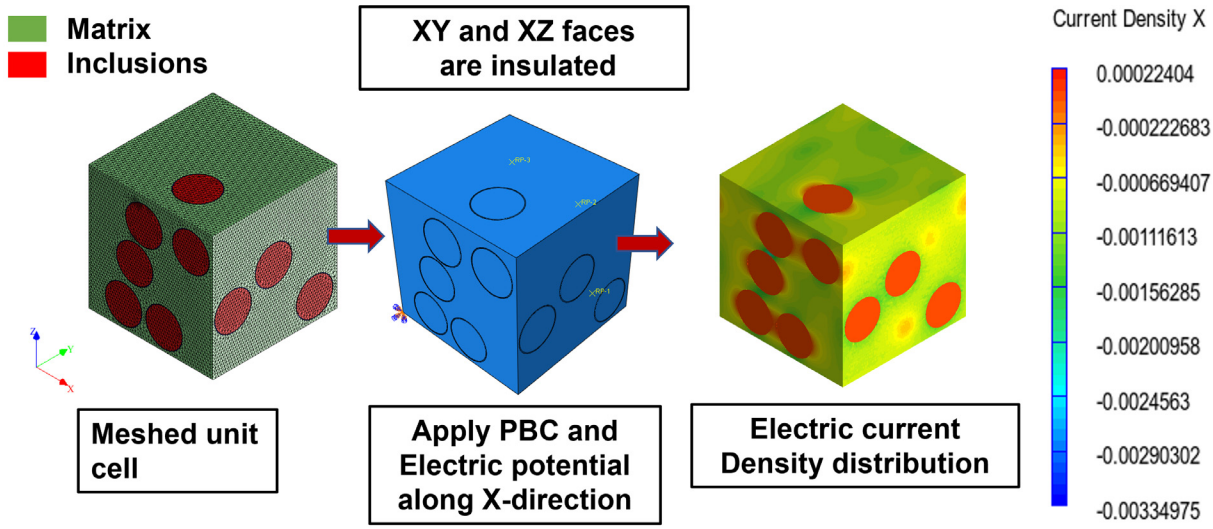

Fig. 4. Schematic representation of the electrical module.

python script and the analysis is carried out using commercial ABAQUS™ software [82]. Table 1 shows the input properties adopted to carry out the mechanical and electrical analysis for the CNT-PSS composite.

2.1.7. Simulation approach for mortars with coated sand inclusions

Here, the RVE microstructures of the coated sand-HCP composite are obtained by generating sand inclusions as solid spheres where no overlapping of the inclusions is allowed. This method is employed following the Lubachhevsky-Stillinger algorithm [77,78]. The volume fraction of sand in this analysis is considered as 45% [37,44]. The median size of the sand particles is adopted as $d_{50} = 600\mu m$ [83], which are dispersed in the unit cell. The randomness of the generated RVEs is ensured by evaluating the randomness of the nearest neighbor distance distributions of the generated inclusions within the RVEs (Please refer to sections B2 and C of the supplementary material). RVE size sensitivity studies were also performed to ensure the representativeness of the generated 3D unit cells. For more details, please refer to sections B2 and C of the supplementary material. The RVE size of 2 mm is selected based on a sensitivity study and any further increase in the size of RVE results in an insignificant change in the responses (Please refer to sections B2 and C of the supplementary material). A variation of thickness for the conductive coating is considered to evaluate the influence of coating thickness. The microstructures are then meshed and PBCs are implemented accordingly as discussed in the previous section. For each case, a mesh convergence study was conducted to obtain optimal mesh for the microstructures. Table 2 shows the input properties adopted to carry out the mechanical and electrical analysis as described earlier in order to evaluate the effective properties of coated sand incorporated HCP matrix. For ITZ, the values for tensile strength (f_t), total fracture energy (G_F) and the Initial fracture energy (G_f) are adopted as 2.7 MPa, 25 N/m and 19 N/m respectively as reported in the literature [44,84,85].

Table 2
Input properties implemented in the sand-coated-HCP composite [44].

Material	Elastic modulus (E) GPa	Poisson's ratio (ν)	Electrical conductivity (κ)
HCP	20 GPa	0.2	0.002 S/m
Conductive Coating	2.46 GPa	0.2	71.3 ± 2.5 S/m
ITZ	10	0.2	0.002 S/m
Sand	60	0.25	10^{-6} S/m

Although strain levels experienced within CNT-PSS coating are lower when compared to its capacity, in the case of the mortar scale, the strain states at the inclusion-HCP matrix interfaces are likely to reach the cracking strain initiating interfacial debonding. This is implemented in this work by adopting a cohesive zone model for the interfacial transition zones (ITZ) at the inclusion-matrix interfaces to define the interfacial debonding behavior at the mortar scale. As such, the interfacial debonding between sand and the HCP matrix plays a major role in the evaluation of the mechanical and electrical responses [44]. This study implements debonding at the matrix-inclusion interfaces by incorporating cohesive zero thickness interface elements and interfacial debonding is implemented using a continuum approach coupled with a cohesive zone model (CZM) [84]. Isotropic damage is incorporated in the matrix so as to obtain the post-peak effective constitutive response of the composite. Such an approach has been successfully implemented for fracture response in particulate-reinforced smart cementitious composites [86], the electro-mechanical response of self-sensing structural materials [44], and dynamic fracture in cementitious materials [87]. In this work, CZM coupled with continuum damage is implemented for interfacial debonding. The zero-thickness interface elements are implemented to ensure continuity in displacement. Such implementation has been successfully modeled for relative slip or separation studies in the literature [44,84]. The mode-I fracture is initiated in the CZM when

Table 1
Input properties incorporated in the CNT-PSS composite [44,69].

Material	Elastic modulus (E)	Poisson's ratio (ν)	Electrical conductivity (κ)	Diameter (D_{CNT})	Length (L_{CNT})
CNT	500 GPa	0.35	10^6 S/m	4 nm	500 nm
PSS	2.4 GPa	0.3	10^{-8}S/m	–	–

the stress state exceeds the tensile strength of the matrix. The traction separation law that governs the damage propagation is obtained by calculating an equivalent interface opening, λ, and equivalent traction, σ_c as shown in Eq. (9) and Eq. (10), respectively [44,84,88].

$$\lambda = \sqrt{\langle [u_n] \rangle^2 + \langle [u_t] \rangle^2} \tag{11}$$

$$\sigma_c = \begin{cases} K_p \lambda, \lambda < \lambda_o \\ f_t \exp\left(-\frac{f_t(\lambda-\lambda_o)}{G_F}\right), \lambda \geq \lambda_o \end{cases} \tag{12}$$

where u_n and u_t are normal and tangential displacement jumps, λ_o is the threshold limit defined by $2G_f/f_t$ (where G_f is the initial fracture energy) up to which the σ_c increases with λ with a penalty stiffness (K_P), f_t is the tensile strength and G_F is the total fracture energy. The volume integral of σ_c is partially differentiated with respect to u_n and u_t to obtain equivalent normal traction (t_{cn}) and tangential traction (t_{ct}). The partial derivatives of the traction with respect to displacement jump defines the mechanical tangent material matrix C_c^u as shown in Eq. (13) [44,84,88].

$$C_c^u = \begin{bmatrix} \frac{\partial t_{cn}}{\partial u_n} & \frac{\partial t_{cn}}{\partial u_n} \\ \frac{\partial t_{cn}}{\partial u_n} & \frac{\partial t_{cn}}{\partial u_n} \end{bmatrix} \tag{13}$$

The mechanical stiffness of each cohesive element is obtained by transforming the tangent material matrix C_c^u to its local coordinate system. When $\lambda \leq \lambda_o$ the traction separation law is governed by K_P whereas when $\lambda > \lambda_o$, the mechanical stiffness matrix is modified at every iteration with increasing λ based on the phenological damage model using a scalar interface damage parameter D_c which is defined as

$$D_c = \frac{\lambda}{\lambda_r} \tag{14}$$

where λ_r corresponds to equivalent interface opening at a very low traction value in the post-peak regime of the traction-separation behavior. λ_r is computed at $0.1f_t$ in the post-peak regime. The approach described herein is implemented in ABAQUS^{TM} via user-subroutine where the initial fracture energy (G_f), total fracture energy (G_F) and tensile strength of the matrix (f_t) are adopted as inputs [84,85]. As explained earlier in Section 2.1.4, the deformed geometry is remeshed and exported to the electrical module. When any interfacial element is damaged, the electrical conductivity of the damaged element is set to zero which prevents any further electric conduction in that element. Such interfacial debonding influences the distribution of current density and strain sensing response in the RVE.

2.2. Machine learning approach

The FE simulation framework presented above is leveraged to generate a large database of strain-dependent FCR values with varying thickness of coating and fraction of coated aggregates for implementation of machine learning-based performance prediction. This paper primarily focuses on neural network (NN), which is discussed in the forthcoming sub-section.

2.2.1. Neural network

A neural network is a mathematical model that maps a given set of predictors, x, to a set of the desired response, y. This mapping between the predictor and the response is comprised of multiple layers of perceptron and activation functions and it is called a feed-forward neural network. The estimated response can be expressed as follows,

$$\boldsymbol{y} = \boldsymbol{f_N}(\boldsymbol{A_N}, \cdots \boldsymbol{f}_2(\boldsymbol{A}_2, \boldsymbol{f}_1(\boldsymbol{A}_1, \boldsymbol{x})) \cdots) \tag{15}$$

where $\boldsymbol{f_N}(\cdot) : \mathbb{R} \rightarrow \mathbb{R}$ is a continuous bounded function which is usually referred to as the activation function, $\boldsymbol{A_i} : \mathbb{R}^{\boldsymbol{d_i}} \rightarrow \mathbb{R}^{\boldsymbol{d_{i+1}}}$ is the transformation matrix that contains weights between two layers of perceptron [89]. The NN has been widely adopted to study the patterns in the data due to the proven universal approximation property, which states that the feed-forward NN architectures with a sigmoid activation function are capable of approximating any set of functions between two Euclidean spaces for the canonical topology [90]. This paper uses sigmoid functions as an activation function since it yields the least error when considering other activations functions such as ReLU, tanh, etc. A similar observation is also reported in the literature [91]. The weights can be solved by formulating the above mapping into a constrained optimization problem as stated below,

$$\boldsymbol{argmin}_{\boldsymbol{A_j}} \{ f_{\boldsymbol{N}}(\boldsymbol{A}_N, \cdots \boldsymbol{f}_2(\boldsymbol{A}_2, (\boldsymbol{f}_1(\boldsymbol{A}_1, \boldsymbol{x})) \cdots) + \lambda \boldsymbol{g}(\mathbf{A_j})) \} \tag{16}$$

where λ is the regularization intensity constant and $g(\cdot)$ is a functional form of the weights to be regularized. The optimization problem is solved by using any optimizing tools and the weights are updated using a backward propagation algorithm.

Due to the non-convexity of the neural network, the solution to this optimization problem is not unique. Moreover, the number of hidden layers and the selection of the number of neurons in each layer affects the result of the regression, and it is subjected to high variance problems when large numbers of neurons and layers are used. As such, proper regularization is needed when NN is implemented. In this study, while training an NN model, a sigmoid function is implemented as an activation function and the Adam algorithm [92] is opted as an optimizer. Fig. 5 shows the schematic diagram of the neural network with the chosen input parameter and the output.

2.2.2. Model tuning and cross-validation

To avoid the possibility of overfitting, a fraction of the data points is kept fully hidden from the models and is used as a test set to evaluate the accuracy and performance of the model on these unseen data. To this end, a k-fold cross-validation (CV) technique is adopted in this study to evaluate the accuracy of the model. To tune the hyperparameters of the model, this study adopts a nested two-level CV approach as detailed in the article by Cawley and Talbot [93]. First, the dataset is split into the training set (which is 80% of the data) and the test set (20% of the data). In outer CV, the model is run for the number of iterations and the average value of the scores (i.e R^2 and MSE), obtained from each fold, is used to compare the performance offered by the ML algorithm. Next, to calculate the proper setting for the hyperparameters from each model, a 5-fold inner CV is implemented within the training set. A similar approach has been successfully adopted to study the composition-dependent mechanical properties using ML techniques [94,95]. To reach an ideal trade-off between accuracy and computational demand, models need to be optimized by tuning the hyperparameters. This can be achieved by gradually increasing the degree of complexity (e.g., number of neurons, number of trees, number of terms, etc.) and tracking the accuracy of the model prediction for both the training and validation datasets. The metrics adopted in this study are mean squared error (MSE) and linear coefficient of determination R^2. The details of the model tuning and validation with the evaluation of the metrics can be found in [96].

2.2.3. Model interpretability

To interpret the ML results, a Shapley Additive Explanations (SHAP)-based model interpretation technique is used in this study [97,98]. The importance of feature 'j' in SHAP for the output of model f, $\phi^j(f)$, is a weighted sum of the feature's contribution of

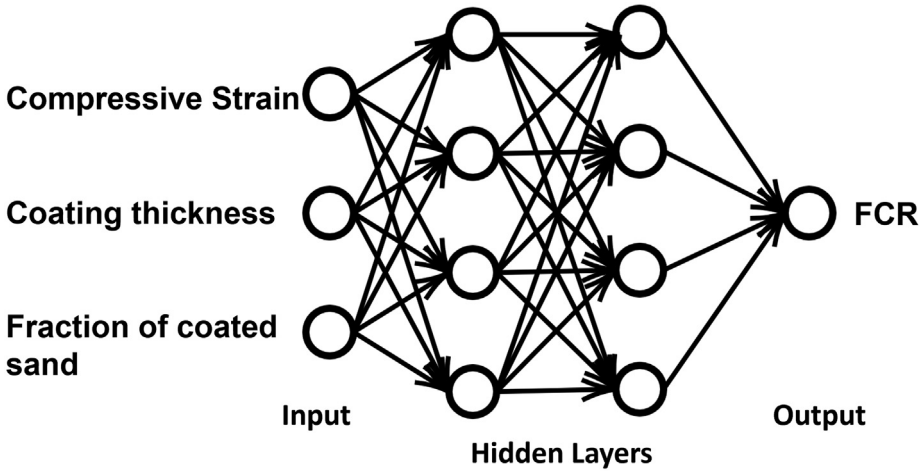

Fig. 5. Schematic diagram of neural network adopted in this paper.

the model's output $f(x_i)$ over all possible feature combinations [99]. $\phi^j(f)$ is expressed as:

$$\phi^j(f) = \sum_{S \sqsubseteq \{x^1,\cdots,x^p\}\{x^j\}} \frac{|S|!(p-|S|-1)!}{p!}\left(f\left(S \bigsqcup \{x^j\}\right) - f(S)\right) \quad (17)$$

where x^j is feature j, S is a subset of features, and p is the number of features in the model.

3. Results and discussions

3.1. Multiscale simulation results

3.1.1. Prediction of effective electro-mechanical response for CNT-PSS nanocomposite

For the CNT-PSS composite, a CNT target volume fraction of 0.035 is obtained based on the percolation studies as shown in section A of the supplementary material. The effective electro-mechanical response of CNT-PSS nanocomposite is obtained following the methodology explained earlier. A strain-dependent conductivity response for the tunneling zone, as reported in [56,60,100], is implemented. Within the tunneling zone, as the strain varies spatially across different elements, the conductivity is mapped to the tunneling zone elements depending on the strain state of each element following the strain-sensitive conductivity response of the tunnel. Thus, for a given externally applied strain, the conductivity varies spatially within the tunneling zones based on the strain-sensitive mapping relationship. The inherent strain sensitivity of the CNTs is considered to be 60, where the variation could be between 1 and 150 as reported in the literature [56,60,101]. The thickness of the tunnels around the CNTs was taken as equal to the radius of CNTs i.e., 2 nm, as per [56,60,69,100]. The electrical simulation applies a unit voltage gradient along X with periodic boundaries along Y and Z [102] to obtain an effective electrical response. For CNT-PSS composite, RVE size-sensitivity and mesh convergence studies are performed to obtain representative and converged solutions. Please refer to section C1 of the supplementary material for more details. From the simulation, under no externally applied strain, a conductivity of 71.25 ± 2.45 S/m was predicted for CNT-PSS coating. For direct comparison, no experimental piezoresistivity data is available for the CNT-PSS composite under compression. For the CNT-epoxy composite, Yin et al. [103] reported the effect of the shape of CNTs on the electrical conductivity of the composite. While the composite with straight nanotubes yielded an experimental electrical conductivity of 65.8S/m, the conductivity for the composite with curved CNTs was 0.00192 S/m [103]. In this study, the CNTs are modeled as straight cylinders and the effective conductivity of the CNT-PSS composite, obtained from the simulation, correlates well with the experimental value for the CNT-epoxy composite. Moreover, an excellent correlation between simulation and experimental values was obtained at the mortar scale, as explained later, which justifies the responses obtained in the CNT-PSS scale.

Fig. 6 shows the computed FCR values with varying strain for the CNT-PSS composite. A linear correlation between the FCR and the strain is observed from Fig. 6, and such correlation can be attributed to the piezoresistive characteristics of the percolated CNT network in the RVE. These mechanically induced deformations alter the current distribution in the RVE leading to an increasing change in the overall resistance of the composite. The piezoresistive responses of CNT-PSS nanocomposite obtained here, serve as input coating property in the analysis of mortars with a varying fraction of coated aggregates. Fig. 7(a) shows the generated meshed microstructure. Fig. 7(b-e) shows the stress distribution and the respective current distributions in the RVE with varying strain. From the stress distributions in Fig. 7(b) and (c), it can be observed that the stresses are concentrated inside the CNTs which can be attributed to the significantly higher stiffness of the CNTs as compared to that of the PSS matrix. Similarly, the electric current density (ECD) distributions in Fig. 7(d) and (e) show that the ECD

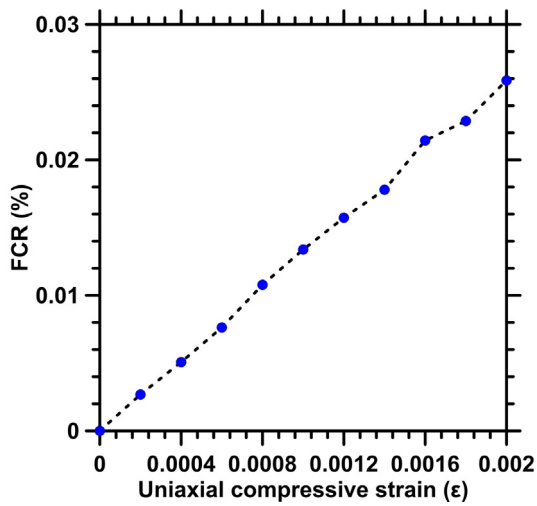

Fig. 6. The fractional change in resistivity with strain for CNT-PSS under compressive strain.

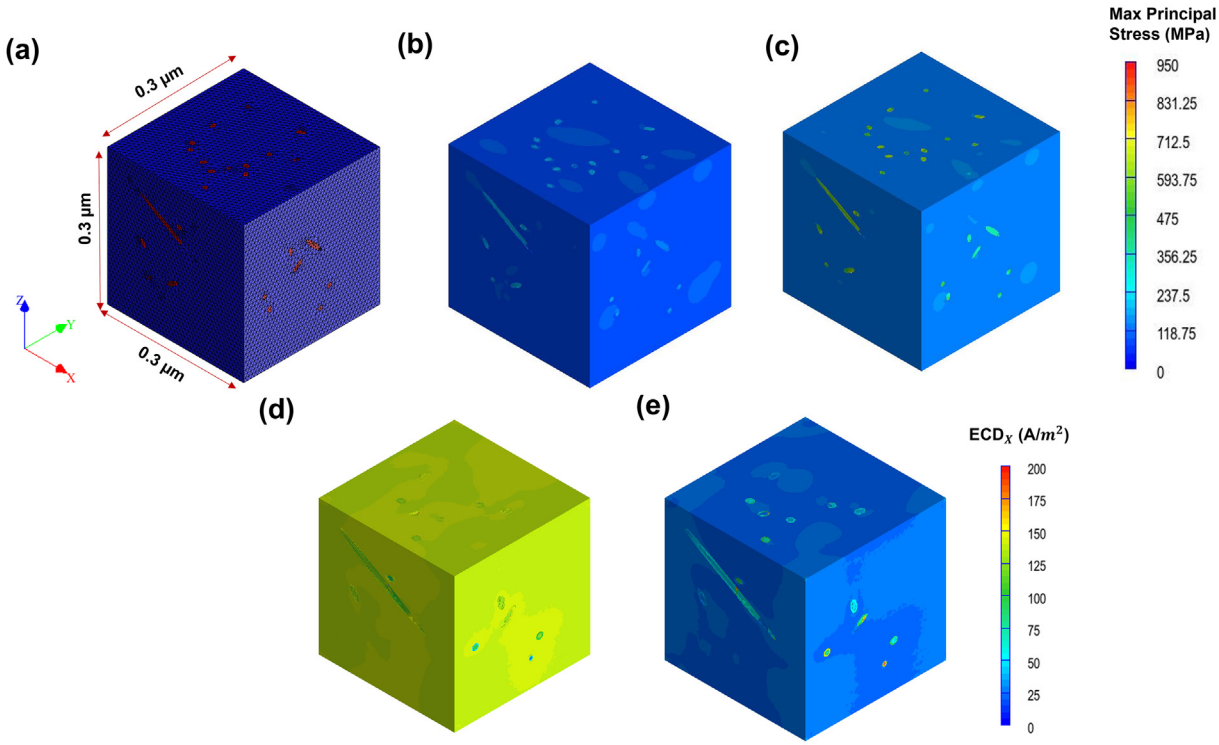

Fig. 7. (a) Representative meshed geometry of CNT-PSS composite. Representative stress state of the CNT-PSS microstructure at a compressive strain of (b) 600 με, (c) 1600 με and the corresponding electric current density for strain equal to (d) 600 με (e) 1600 με.

is more concentrated inside the CNTs as compared to the PSS matrix which can be attributed to the significantly higher electrical conductivity of the CNTs as compared to the PSS matrix. Overall, with increasing strain, the state of stress in the RVE increases, and consequently it alters the resistivity of the microstructure due to the change in the conductivity path.

3.1.2. Prediction of strain sensing ability of nano-engineered smart mortar

This section describes the application of the framework to the smart self-sensing cementitious material enabled through nano-engineered cement aggregate interfaces [37–41,104]. The electromechanical response of the CNT-PSS nanocomposite serves as input property for the coating in this scale. The forthcoming subsections describe the application of the electro-mechanical simulation framework to explore the influence of coating thickness and the fraction of coated sand on the electromechanical behavior of the composite. In addition, this study also compares the numerical simulation results with the experimental value reported in the literature [37] for the smart self-sensing cementitious material for validation. As described earlier, a mechanical module is first implemented on the generated unit cell (Fig. 8(a)). The generated microstructure unit cell is meshed, and a periodic boundary is applied, followed by the displacement-controlled simulation to obtain the deformed unit cell. To obtain representative and converged solutions at the mortar scale, RVE size-sensitivity and mesh convergence studies are conducted. Please refer to section C2 of the supplementary material for more details. The volume fraction of sand inclusion is taken as 45% [44]. The fraction of coated sand particles ranges in between 20%−100%. Such mortars with such a fraction of coated sand particles are able to form percolated paths for electric conduction. Please refer to section A.2 of the supplementary material for more details on percolation studies in the mortar scale.

The median size of sand inclusions is considered as 600 μm[44] and sand inclusions are dispersed randomly in the unit cell with an edge length of 2 *mm*. The size of the unit cell is selected based on the sensitivity studies as detailed in the section C of the supplementary material. Similar relative RVE with identical inclusion size has also been implemented [44] to evaluate micromechanical responses of cementitious composites. In this study, the interfacial transition zone (ITZ) is also incorporated around the sand particles. The interfacial debonding is modeled by employing a cohesive zone model (CZM) [88] where zero thickness interfacial elements are implemented at the conductive coating-ITZ interface as explained earlier in this paper. The traction separation law in CZM is defined by tensile strength (t_f), total fracture energy (G_F) and initial fracture energy (G_f) as described in Section 2.1.7. The values of these parameters are obtained from our previous study [44]. Initially, the values of the scalar interface damage parameters (D_c) is taken as zero. With increasing strain, the scalar value gradually increases to 1 which denotes that the element is completely damaged. The unit cell is finely meshed using C3D10 elements in ABAQUS^{TM}.

The deformed geometry due to mechanical loading is imported to the re-meshing module to refine the mesh, ensuring a good quality of elements. The re-meshed unit cell is then imported to an electrical module for electrical analysis. In the electrical module, the faces parallel to the x-axis are insulated, and a unit potential difference is applied along the x-axis to obtain ECD and electric field in the unit cell. The post-processing module involves the computation of the FCR, as explained earlier. Fig. 8(b-c) shows the stress state of the unit cell under the applied compressive strain of 27 με and 170 με respectively. The corresponding ECD distribution is shown in Fig. 9(d-e). Due to the piezoresistive behavior of the conductive coating, the ECDs are altered, resulting in a change in the characteristic of the electrical response in the unit cell with an increase in compressive strain.

To validate the prediction of strain sensing behavior of the smart cementitious material containing nano-engineered cement aggregate interface under compression, Fig. 9 draws a comparison between the numerical analysis results and the experimental results reported in an experimental study [37].

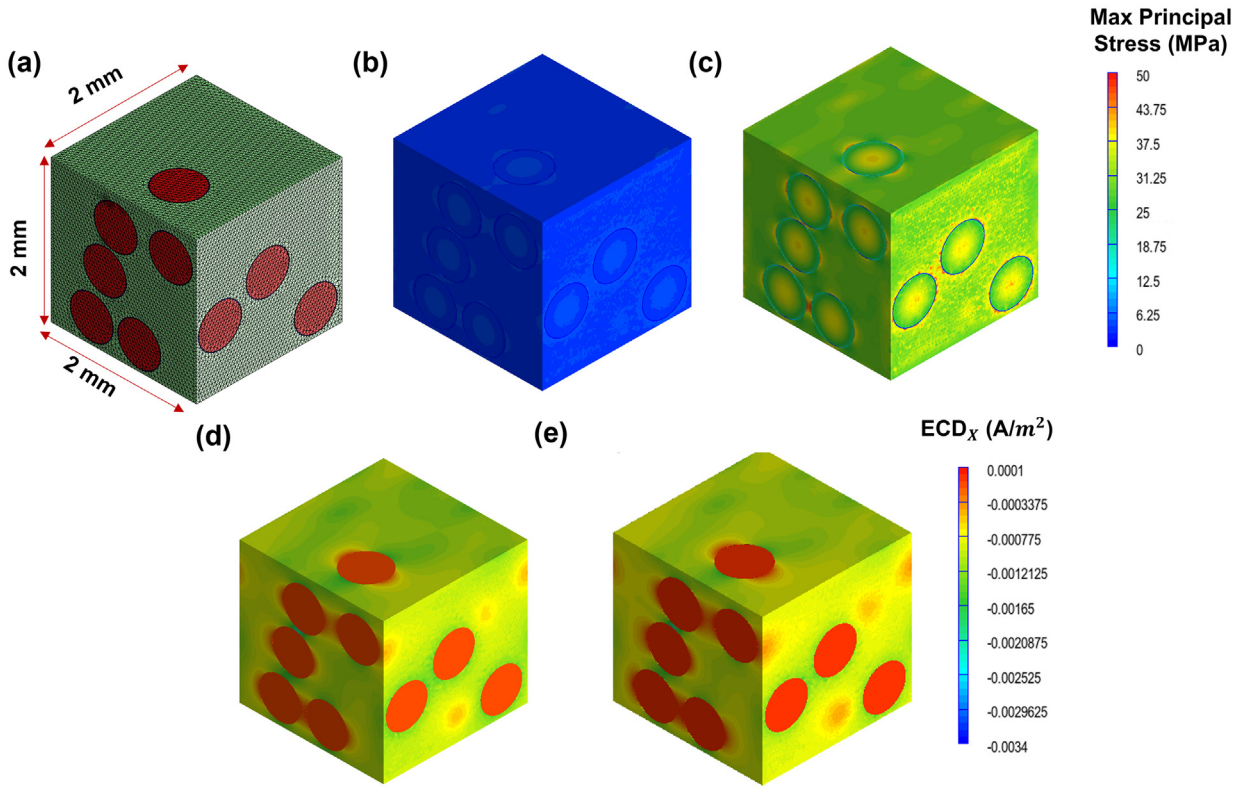

Fig. 8. (a) Generated and meshed sand-coated microstructure. Representative stress state of the sand-coated-hcp microstructure at a compressive strain of (b) 27 με (c) 170 με and the corresponding electric current density for strain equal to (d) 27 με (e) 170 με.

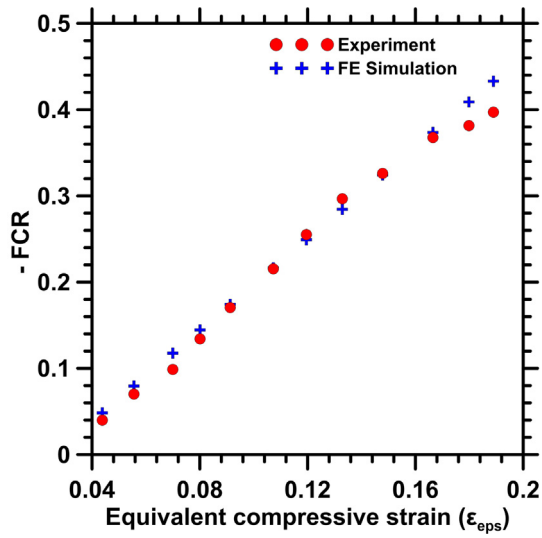

Fig. 9. Simulated piezoresistivity of a sand-coated cement mortar for compressive strain compared with the experimental values reported in an experimental study [37].

A good correlation is achieved between the numerical analysis and the experimental results. This verifies the efficacy of the numerical approach adopted here. While Fig. 9 highlights the strain sensing capability of the smart material, Fig. 10 illustrates the influence of the thickness of the coating and the fraction of coated aggregates on the overall sensing efficiency.

Fig. 10(a) shows the influence of the thickness of the coating on the FCR while the fraction of coated aggregates is fixed at 100% and strains are varied. From Fig. 10(a), it is observed that the FCR increases with an increase in coating thickness for all the applied strains. However, the rate of increase in FCR with respect to the increase in coating thickness decreases beyond a thickness of 20 μm. Such trend can be attributed to the fact that for a coating thickness of 20 μm the coating surfaces from neighboring inclusions almost overlap thereby achieving maximum strain sensitivity. Thus, any further increase in the coating thickness beyond 20 μm does not alter the connected path significantly which is reflected in the form of no significant improvement in FCR beyond a coating thickness of 20 μm. Similar observations are reported in the literature for composites with conductive phases embedded in non-conductive matrices [105,106]. It is observed that a thin conductive film of around 10–20 μm is sufficient to obtain an efficient strain-sensing ability in these materials. Fig. 10(b) shows the variation of the FCR with the fraction of coated sand particles. Here, the thickness of the coating is fixed at 10 μm and the strains are varied. For every simulation, 10 different randomly generated RVEs are considered, and the mean value of FCR is obtained. The general trend in Fig. 10(b) suggests that the FCR increases with increasing fraction of coated aggregates. However, with a coating fraction beyond 80%, no significant change in FCR is observed with an increasing fraction of coated aggregates.

While the above responses show a significant variation of FCR with change in coating thickness and fraction of coated sand particles, the forthcoming section leverages the electromechanical simulation framework to develop a large dataset that is required for ML implementation.

3.2. Machine learning-based performance prediction

3.2.1. Dataset generation

The sequentially coupled simulation technique illustrated earlier is exploited to generate the electromechanical response of

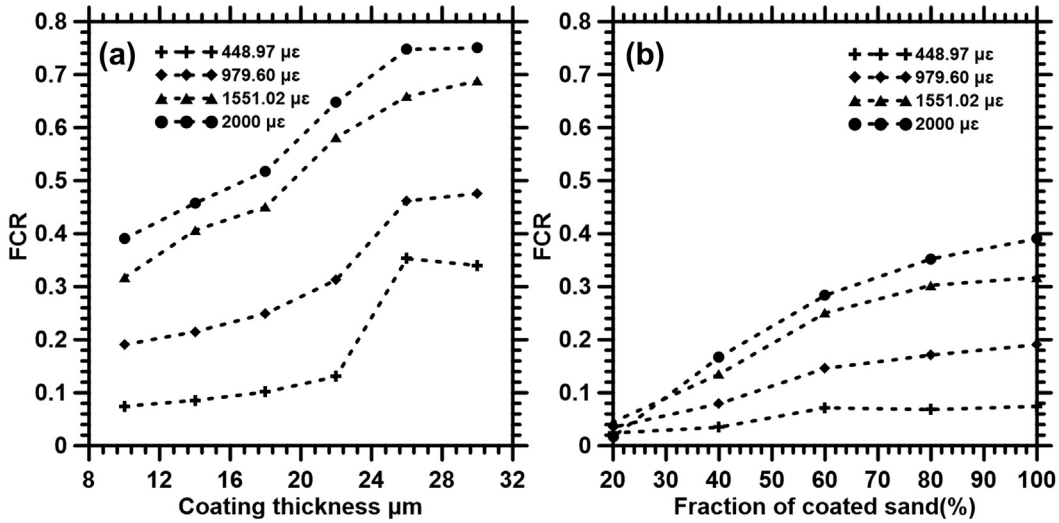

Fig. 10. (a) Variation of FCR with varying thickness of the coating for the case of 100% coated aggregates; (b) relationship between FCR and the fraction of coated sand inclusions for a coating thickness of 10 μm under varying applied strain.

the RVEs. Under variable strain, multiple combinations are employed by linearly varying the fraction of coated sand (20% to 100%) and the thickness of the coating (10 μm to 30 μm). This information is used as training data for machine learning prediction. While this study implements input parameters such as coating thickness, the fraction of coated sand, and compressive strain as a starting point, it needs to be noted that the influence of other parameters such as CNT dosage, selection of polymer matrix material for the coating, variations in the size distribution of sand inclusions, longevity, or bonding characteristics of the coating, etc. and their relative sensitivity in the light of strain sensing ability of the composite, can be incorporated in the future to improve the generalizability and robustness of the model.

For adequacy, the database generated for ML should be (i) balanced, (ii) representative, (iii) complete, and (iv) consistent [95]. In the current study, the dataset is generated by varying the thickness of the coating and the fraction of coated sand particles in a uniform fashion. This is to ensure that the data points from all possible ranges are equally represented. For the representativeness of the dataset, the data are split into training (80%) and test set (20%). The hyperparameters are tuned by implementing 5-fold cross-validation. At every fold in cross-validation, the training data is further divided into 80% of the training set and 20% for validation. The errors (training error and validation error) calculated from each fold are averaged to represent the average model error. The completeness of the dataset is ensured here by choosing all the possible ranges of the coating thickness and fraction of coated sand observed experimentally. Moreover, the consistency of the dataset is carefully maintained by following the analysis on RVE, loading conditions, and evaluation of piezoresistive procedure within the electro-mechanical simulation for all the RVEs generated. Thus, the overall adequacy of the dataset is ensured by careful implementation of all the four above-mentioned criteria during the dataset generation and model training/testing procedure. In this study, the dataset consists of 3000 pairs of inputs and output vectors. The dataset was divided into an 80:20 ratio, where 80% of the dataset was used for the train set and the remaining 20% for the test set. The test set is kept hidden from the network during training. A sigmoid function is used as the activation function on the hidden layers. For more details on the dataset adequacy, please refer to section E of the supplementary material.

3.2.2. Prediction from trained neural network

The choice of the NN hidden layers and neurons in each layer was based on the hyperparameter optimization where a trade-off between the minimum *MSE* and maximum R^2 was obtained. Fig. 12 shows the *MSE* and R^2 values with an increasing number of neurons for hidden layers equal to 2. It is observed from Fig. 11(a) that that the MSE drops as the number of neurons is

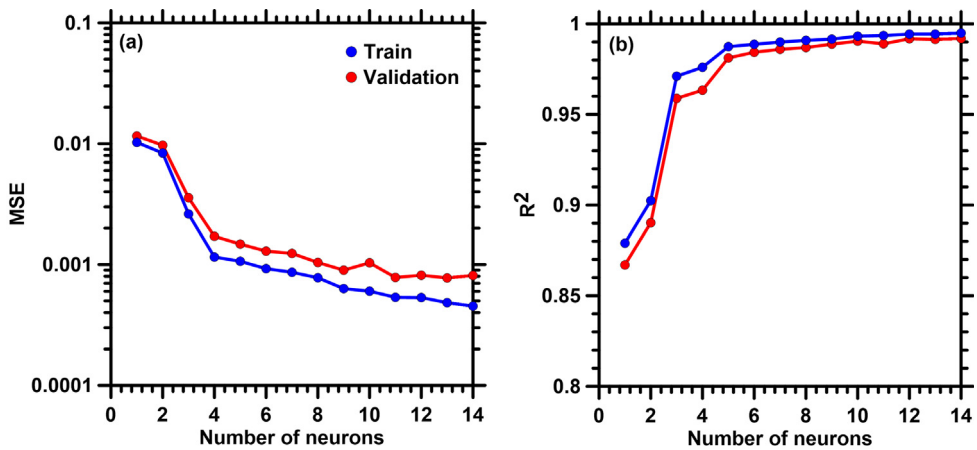

Fig. 11. (a) MSE value an (b) R^2 value of the neural network model with respect to hidden nodes for a hidden layer equal to 2.

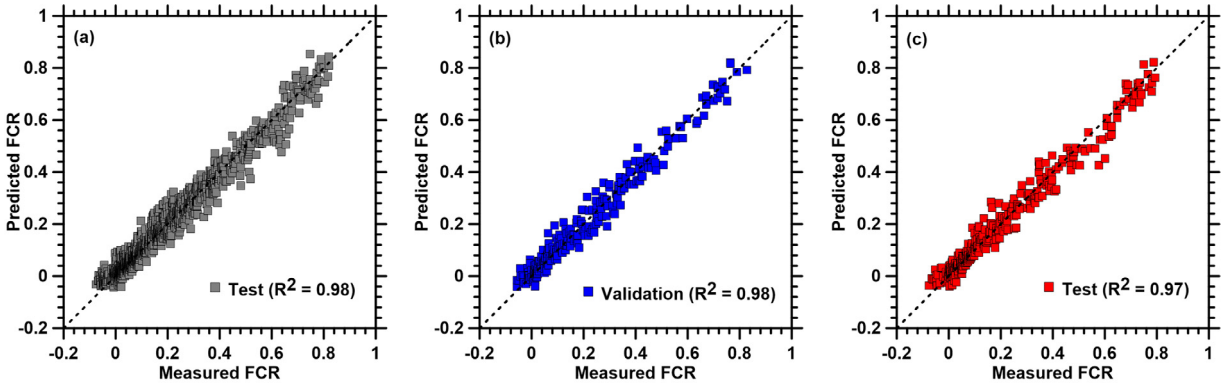

Fig. 12. Comparison of the measured FCR from the FE model with the predicted FCR from the trained NN model using (a) test set, (b) validation set, and (c) test set of data.

increased and beyond a neuron number of 11, the MSE for the validation set almost converges to a constant value. Similarly, for the same number of neurons, the R^2 value also gets saturated as shown in Fig. 11(b) and any increase in the number of neurons beyond 11 does not make any significant change to the R^2 values. Hence, the number of neurons equal to 11 is selected for this study.

The network was trained using TensorFlow [107], where the optimal weight matrices and bias arrays are obtained by minimizing the MSE between the true value (prediction from FE simulations) and the predicted value from NN. Such optimization was performed via backpropagation, using the Adam algorithm. The network was converged for a learning rate equal to 0.001 and 500 epochs.

To check the accuracy of the optimized NN, the predicted values from NN are compared with the measured values from multiscale simulations for the training, validation, and test dataset as shown in Fig. 12.

While an R^2 value of 0.98 is observed for training and validation datasets, an excellent correlation is obtained with a R^2 value of 0.97 for the test dataset that was not seen by the NN model during training and validation, as shown in Fig. 12. It needs to be noted that the prediction accuracy of the ML models presented here is only evaluated within the range of parameters considered within this study. As such, detailed extrapolation studies are needed to assess the prediction accuracy and associated uncertainties when the values of the input parameters go beyond the ranges considered in this study.

3.2.3. Insights from the NN model

This section demonstrates the interpretability of the NN predictions by using SHAP [97]. In SHAP, the impact of each feature on the prediction is obtained by assigning each feature an importance value for a respective prediction. The result shown in Fig. 13 demonstrates that the FCR is dominated by the coating thickness, followed by the strain and the fraction of coated sand present in the system. In other words, for a given strain, coating thickness shows more influence on the FCR than the fraction of coated aggregates. Such inferences can significantly influence the strategies to optimize these smart mortar systems for enhanced strain-sensing efficiency.

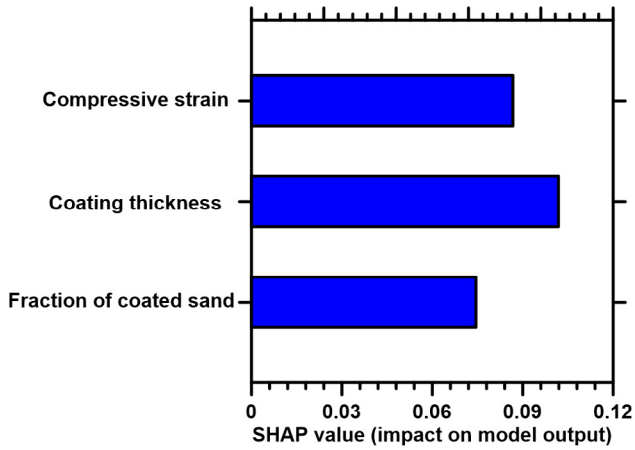

Fig. 13. SHAP values for each input from the trained NN model.

4. Conclusion

This paper presents a comprehensive approach toward the prediction of electromechanical response and strain sensing ability of a smart cementitious composite. A multiscale approach is implemented to obtain the electro-mechanical behavior of the nano-engineered CNT-based coating which serves as the input coating property for the electro-mechanical simulation of the mortar. The electro-mechanical simulation adopted herein followed a sequential approach where the mechanical module is initiated to obtain the deformed geometry and then re-meshed before exporting to an electrical module to compute the change in resistance at different strain values. The efficacy of the simulation is evaluated by comparing the simulated responses with the experimental results available in the literature, where a good correlation is obtained. Such good correlation enables confidence in the ability of the simulation methodology to represent the complex hierarchical structure of the smart cementitious composite with thin-film coating effectively. The validated Numerical framework is used to evaluate the influence of coating thickness and the fraction of coated aggregates towards strain-sensing efficiency. The results suggest that the FCR increases as the coating thickness is increased and the trend continues till a coating thickness of 20 μm is reached beyond

which the FCR tends to saturate and no significant increase in FCR is observed when the coating thickness is increased beyond 20 μm. Such trend can be attributed to the fact that for a coating thickness of 20 μm the coating surfaces from neighboring inclusions almost overlap thereby achieving maximum strain sensitivity. Any further increase in the coating thickness does not alter the connected path significantly which is reflected in the form of no significant improvement in FCR beyond a coating thickness of 20 μm. Similar trends are observed when the fraction of coated sand inclusions is varied where the rate of increase in FCR decreases progressively with an increasing fraction of coated sand. The validated simulation framework is also leveraged to build a large, consistent, and representative database of strain-dependent FCR by varying the coating thickness and fraction of coated sand particles. The large database is used to build an NN-based predictive model. By judiciously selecting the optimal parameters, an optimal trade-off between the level of complexity and accuracy is obtained while ensuring there is no under-or overfitting. Excellent prediction efficacy is obtained using 11 neurons and 2 hidden layers. To interpret the NN predictions, SHAP values are also computed for all the input parameters to elucidate their relative influence on the FCR values From the SHAP values, after considering all the possible combinations that evaluate the importance of each model features on the model's output, for a given strain, the coating thickness showed a higher influence on the obtained FCR than the fraction of coated sand. Overall, synergistically integrated multiscale FE simulation with ML approach, presented in this paper can be used as a starting point for designing a wide range of strain-sensing materials for multifunctional applications.

Declaration of Competing Interest

The authors declare that they have no known competing financial interests or personal relationships that could have appeared to influence the work reported in this paper.

Acknowledgements

This research was conducted in the Multiscale & Multiphysics Mechanics of Materials Research Laboratory (M4RL) at the University of Rhode Island and the supports that have made this laboratory possible are acknowledged. The authors acknowledge Bluewaves and Andromeda High-Performance Research Computing at the University of Rhode Island (URI) for providing computer clusters and data storage resources that have contributed to the research results reported within this paper.

Data availability

The raw data required to reproduce these findings are available to download from.

https://github.com/glyngdoh/Simulated-Data-Strain-Sensing-Response-of-a-Nano-engineered-Smart-Cementitious-Composite.git.

Appendix A. Supplementary material

Supplementary data to this article can be found online at https://doi.org/10.1016/j.matdes.2021.109995.

References

[1] C.R. Farrar, K. Worden, An introduction to structural health monitoring, Philos. Trans. Royal Soc. A: Math., Phys. Eng. Sci. 365 (2007) 303–315, https://doi.org/10.1098/rsta.2006.1928.

[2] S.W. Doebling, C.R. Farrar, M.B. Prime, A summary review of vibration-based damage identification methods, identification methods, The Shock and Vibration Digest 30 (1998) 91–105.

[3] J.m. w Brownjohn, Structural health monitoring of civil infrastructure, Philos. Trans. Royal Soc. A: Math., Phys. Eng. Sci. 365 (2007) 589–622. https://doi.org/10.1098/rsta.2006.1925.

[4] J.M. Ko, Y.Q. Ni, Technology developments in structural health monitoring of large-scale bridges, Eng. Struct. 27 (2005) 1715–1725, https://doi.org/10.1016/j.engstruct.2005.02.021.

[5] P.C. Chang, A. Flatau, S.C. Liu, Review paper: health monitoring of civil infrastructure, Structural Health Monitoring 2 (2003) 257–267, https://doi.org/10.1177/1475921703036169.

[6] W. Hong, J. Zhang, G. Wu, Z. Wu, Comprehensive comparison of macro-strain mode and displacement mode based on different sensing technologies, Mech. Syst. Sig. Process. 50–51 (2015) 563–579, https://doi.org/10.1016/j.ymssp.2014.05.011.

[7] D.G. Aggelis, A.S. Paipetis, Monitoring of resin curing and hardening by ultrasound, Constr. Build. Mater. 26 (2012) 755–760, https://doi.org/10.1016/j.conbuildmat.2011.06.084.

[8] R. Yang, H. Zhang, T. Li, Y. He, An investigation and review into microwave thermography for NDT and SHM, IEEE Far East NDT New Technology Application Forum (FENDT) 2015 (2015) 133–137, https://doi.org/10.1109/FENDT.2015.7398326.

[9] M. Strantza, D.G. Aggelis, D. De Baere, P. Guillaume, D. Van Hemelrijck, Evaluation of SHM system produced by additive manufacturing via acoustic emission and other NDT methods, Sensors 15 (2015) 26709–26725, https://doi.org/10.3390/s151026709.

[10] K.T. Tan, N. Watanabe, Y. Iwahori, X-ray radiography and micro-computed tomography examination of damage characteristics in stitched composites subjected to impact loading, Compos. B Eng. 42 (2011) 874–884, https://doi.org/10.1016/j.compositesb.2011.01.011.

[11] S. Das, P. Saha, A review of some advanced sensors used for health diagnosis of civil engineering structures, Measurement 129 (2018) 68–90, https://doi.org/10.1016/j.measurement.2018.07.008.

[12] S. Taheri, A review on five key sensors for monitoring of concrete structures, Constr. Build. Mater. 204 (2019) 492–509, https://doi.org/10.1016/j.conbuildmat.2019.01.172.

[13] B. Han, L. Zhang, J. Ou, Smart and multifunctional concrete toward sustainable infrastructures, Springer Singapore (2017), https://doi.org/10.1007/978-981-10-4349-9.

[14] B. Han, S. Ding, X. Yu, Intrinsic self-sensing concrete and structures: A review, Measurement 59 (2015) 110–128, https://doi.org/10.1016/j.measurement.2014.09.048.

[15] S. Ding, S. Dong, A. Ashour, B. Han, Development of sensing concrete: Principles, properties and its applications, J. Appl. Phys. 126 (2019), https://doi.org/10.1063/1.5128242 241101.

[16] L. Hui, O. Jinping, Structural health monitoring: from sensing technology stepping to health diagnosis, Procedia Eng. 14 (2011) 753–760, https://doi.org/10.1016/j.proeng.2011.07.095.

[17] E.P. Carden, P. Fanning, Vibration based condition monitoring: a review, Structural Health Monitoring 3 (2004) 355–377, https://doi.org/10.1177/1475921704047500.

[18] Y.Y. Li, Hypersensitivity of strain-based indicators for structural damage identification: A review, Mech. Syst. Sig. Process. 24 (2010) 653–664, https://doi.org/10.1016/j.ymssp.2009.11.002.

[19] D. Feng, M.Q. Feng, Experimental validation of cost-effective vision-based structural health monitoring, Mech. Syst. Sig. Process. 88 (2017) 199–211, https://doi.org/10.1016/j.ymssp.2016.11.021.

[20] T.-H. Yi, H.-N. Li, Innovative structural health monitoring technologies, Measurement 88 (2016) 343–344, https://doi.org/10.1016/j.measurement.2016.05.038.

[21] S. Kekez, J. Kubica, Connecting concrete technology and machine learning: proposal for application of ANNs and CNT/concrete composites in structural health monitoring, RSC Adv. 10 (2020) 23038–23048, https://doi.org/10.1039/D0RA03450A.

[22] P.-W. Chen, D.D.L. Chung, Carbon fiber reinforced concrete for smart structures capable of non-destructive flaw detection, Smart Mater. Struct. 2 (1993) 22, https://doi.org/10.1088/0964-1726/2/1/004.

[23] F. Azhari, N. Banthia, Cement-based sensors with carbon fibers and carbon nanotubes for piezoresistive sensing, Cem. Concr. Compos. 34 (2012) 866–873, https://doi.org/10.1016/j.cemconcomp.2012.04.007.

[24] M.S. Konsta-Gdoutos, C.A. Aza, Self sensing carbon nanotube (CNT) and nanofiber (CNF) cementitious composites for real time damage assessment in smart structures, Cem. Concr. Compos. 53 (2014) 162–169, https://doi.org/10.1016/j.cemconcomp.2014.07.003.

[25] B. Han, X. Yu, K. Zhang, E. Kwon, J. Ou, Sensing properties of CNT-filled cement-based stress sensors, J. Civil Struct. Health Monit. 1 (2011) 17–24, https://doi.org/10.1007/s13349-010-0001-5.

[26] H.K. Kim, I.S. Park, H.K. Lee, Improved piezoresistive sensitivity and stability of CNT/cement mortar composites with low water–binder ratio, Compos. Struct. 116 (2014) 713–719, https://doi.org/10.1016/j.compstruct.2014.06.007.

[27] L. Coppola, A. Buoso, F. Corazza, Comparative evaluation of piezoresistivity of CNTs/Cement composites measured by AC and DC techniques, Thirteen International Conference on Recent Advances in Concrete Technology and Sustainability Issues, 2015.

[28] S. Sun, S. Ding, B. Han, S. Dong, X. Yu, D. Zhou, J. Ou, Multi-layer graphene-engineered cementitious composites with multifunctionality/intelligence, Compos. B Eng. 129 (2017) 221–232, https://doi.org/10.1016/j.compositesb.2017.07.063.

[29] B.G. Han, B.Z. Han, X. Yu, Effects of the content level and particle size of nickel powder on the piezoresistivity of cement-based composites/sensors, Smart Mater. Struct. 19 (2010), https://doi.org/10.1088/0964-1726/19/6/065012 065012.

[30] S. Zhu, D.D.L. Chung, Analytical model of piezoresistivity for strain sensing in carbon fiber polymer–matrix structural composite under flexure, Carbon 45 (2007) 1606–1613, https://doi.org/10.1016/j.carbon.2007.04.012.

[31] S. Wen, D.D.L. Chung, Model of piezoresistivity in carbon fiber cement, Cem. Concr. Res. 36 (2006) 1879–1885, https://doi.org/10.1016/j.cemconres.2006.03.029.

[32] S. Wen, D.D.L. Chung, A comparative study of steel- and carbon-fibre cement as piezoresistive strain sensors, Adv. Cem. Res. 15 (2003) 119–128, https://doi.org/10.1680/adcr.2003.15.3.119.

[33] S. Wen, D.D.L. Chung, Piezoresistivity in continuous carbon fiber cement-matrix composite, Cem. Concr. Res. 29 (1999) 445–449, https://doi.org/10.1016/S0008-8846(98)00211-7.

[34] X. Wang, D.D.L. Chung, Short carbon fiber reinforced epoxy coating as a piezoresistive strain sensor for cement mortar, Sens. Actuators, A 71 (1998) 208–212, https://doi.org/10.1016/S0924-4247(98)00187-3.

[35] S. Wang, D.D.L. Chung, Piezoresistivity in continuous carbon fiber polymer-matrix composite, Polym. Compos. 21 (2000) 13–19, https://doi.org/10.1002/pc.10160.

[36] D.D.L. Chung, Piezoresistive cement-based materials for strain sensing, J. Intell. Mater. Syst. Struct. 13 (2002) 599–609, https://doi.org/10.1106/104538902031861.

[37] K.J. Loh, J. Gonzalez, Cementitious composites engineered with embedded carbon nanotube thin films for enhanced sensing performance, J. Phys.: Conf. Ser. 628 (2015), https://doi.org/10.1088/1742-6596/628/1/012042 012042.

[38] S. Gupta, J.G. Gonzalez, K.J. Loh, Self-sensing concrete enabled by nano-engineered cement-aggregate interfaces, Structural Health Monitoring 16 (2017) 309–323, https://doi.org/10.1177/1475921716643867.

[39] S. Gupta, J. Gonzalez, K.J. Loh, Damage detection using smart concrete engineered with nanocomposite cement-aggregate interfaces, Structural Health Monitoring 2015. 0 (2015). http://www.dpi-proceedings.com/index.php/SHM2015/article/view/1037 (accessed November 17, 2020).

[40] K.J. Loh, J.P. Lynch, N.A. Kotov, Mechanical-electrical characterization of carbon-nanotube thin films for structural monitoring applications, in: Smart Structures and Materials 2006: Sensors and Smart Structures Technologies for Civil, Mechanical, and Aerospace Systems, International Society for Optics and Photonics, 2006, p. 61741Z, https://doi.org/10.1117/12.658896.

[41] J. Gonzalez, S. Gupta, K.J. Loh, R. Wu, N. Garg, Nano-engineered Cementitious Composites and Electrical Impedance and Electrical Impedance Tomography for Spatial Damage Detection, in: 2016. https://trid.trb.org/view/1393239 (accessed October 23, 2020).

[42] B. Loyola, A.R. Burton, K.J. Loh, Modeling the Resistivity of CNT Thin Films., Sandia National Laboratories, 2012. https://www.osti.gov/biblio/1072508 (accessed October 23, 2020).

[43] B.M. Lee, S. Gupta, K.J. Loh, S. Nagarajaiah, 13 - Strain sensing and structural health monitoring using nanofilms and nanocomposites, in: K.J. Loh, S. Nagarajaiah (Eds.), Innovative Developments of Advanced Multifunctional Nanocomposites in Civil and Structural Engineering, Woodhead Publishing, Oxford, 2016, pp. 303–326, https://doi.org/10.1016/B978-1-78242-326-3.00013-0.

[44] S. Nayak, S. Das, A microstructure-guided numerical approach to evaluate strain sensing and damage detection ability of random heterogeneous self-sensing structural materials, Comput. Mater. Sci. 156 (2019) 195–205, https://doi.org/10.1016/j.commatsci.2018.09.035.

[45] S. Gong, Z.H. Zhu, On the mechanism of piezoresistivity of carbon nanotube polymer composites, Polymer 55 (2014) 4136–4149, https://doi.org/10.1016/j.polymer.2014.06.024.

[46] S. Gong, Z.H. Zhu, E.I. Haddad, Modeling electrical conductivity of nanocomposites by considering carbon nanotube deformation at nanotube junctions, J. Appl. Phys. 114 (2013), https://doi.org/10.1063/1.4818478 074303.

[47] S. Gong, Z.H. Zhu, S.A. Meguid, Carbon nanotube agglomeration effect on piezoresistivity of polymer nanocomposites, Polymer 55 (2014) 5488–5499, https://doi.org/10.1016/j.polymer.2014.08.054.

[48] N. Hu, Y. Karube, M. Arai, T. Watanabe, C. Yan, Y. Li, Y. Liu, H. Fukunaga, Investigation on sensitivity of a polymer/carbon nanotube composite strain sensor, Carbon 48 (2010) 680–687, https://doi.org/10.1016/j.carbon.2009.10.012.

[49] F. Dalmas, R. Dendievel, L. Chazeau, J.-Y. Cavaillé, C. Gauthier, Carbon nanotube-filled polymer composites. Numerical simulation of electrical conductivity in three-dimensional entangled fibrous networks, Acta Materialia 54 (2006) 2923–2931, https://doi.org/10.1016/j.actamat.2006.02.028.

[50] N. Hu, Z. Masuda, G. Yamamoto, H. Fukunaga, T. Hashida, J. Qiu, Effect of fabrication process on electrical properties of polymer/multi-wall carbon nanotube nanocomposites, Compos. A Appl. Sci. Manuf. 39 (2008) 893–903, https://doi.org/10.1016/j.compositesa.2008.01.002.

[51] A. Hallal, R. Younes, F. Fardoun, Review and comparative study of analytical modeling for the elastic properties of textile composites, Compos. B Eng. 50 (2013) 22–31, https://doi.org/10.1016/j.compositesb.2013.01.024.

[52] J.-M. Yang, C.-L. Ma, T.-W. Chou, Fiber inclination model of three-dimensional textile structural composites, J. Compos. Mater. 20 (1986) 472–484, https://doi.org/10.1177/002199838602000505.

[53] G.M. Koo, T.N. Tallman, Higher-order resistivity-strain relations for self-sensing nanocomposites subject to general deformations, Compos. B Eng. 190 (2020), https://doi.org/10.1016/j.compositesb.2020.107907 107907.

[54] S. Jacques, I. De Baere, W. Van Paepegem, Application of periodic boundary conditions on multiple part finite element meshes for the meso-scale homogenization of textile fabric composites, Compos. Sci. Technol. 92 (2014) 41–54, https://doi.org/10.1016/j.compscitech.2013.11.023.

[55] J. Gager, H.E. Pettermann, Numerical homogenization of textile composites based on shell element discretization, Compos. Sci. Technol. 72 (2012) 806–812, https://doi.org/10.1016/j.compscitech.2012.02.009.

[56] A.K. Chaurasia, G.D. Seidel, Computational micromechanics analysis of electron-hopping-induced conductive paths and associated macroscale piezoresistive response in carbon nanotube–polymer nanocomposites, J. Intell. Mater. Syst. Struct. 25 (2014) 2141–2164, https://doi.org/10.1177/1045389X13517314.

[57] A.K. Chaurasia, X. Ren, G.D. Seidel, Computational micromechanics analysis of electron hopping and interfacial damage induced piezoresistive response in carbon nanotube-polymer nanocomposites, Smart Mater. Struct. 23 (2014), https://doi.org/10.1088/0964-1726/23/7/075023 075023.

[58] A.I. Oliva-Avilés, F. Avilés, G.D. Seidel, V. Sosa, On the contribution of carbon nanotube deformation to piezoresistivity of carbon nanotube/polymer composites, Compos. B Eng. 47 (2013) 200–206, https://doi.org/10.1016/j.compositesb.2012.09.091.

[59] X. Ren, G.D. Seidel, Computational micromechanics modeling of inherent piezoresistivity in carbon nanotube–polymer nanocomposites, J. Intell. Mater. Syst. Struct. 24 (2013) 1459–1483, https://doi.org/10.1177/1045389X12471442.

[60] X. Ren, A.K. Chaurasia, A.I. Oliva-Avilés, J.J. Ku-Herrera, G.D. Seidel, F. Avilés, Modeling of mesoscale dispersion effect on the piezoresistivity of carbon nanotube-polymer nanocomposites via 3D computational multiscale micromechanics methods, Smart Mater. Struct. 24 (2015), https://doi.org/10.1088/0964-1726/24/6/065031 065031.

[61] A.R. Alian, S.I. Kundalwal, S.A. Meguid, Multiscale modeling of carbon nanotube epoxy composites, Polymer 70 (2015) 149–160, https://doi.org/10.1016/j.polymer.2015.06.004.

[62] E. Stora, B. Bary, Q.-C. He, E. Deville, P. Montarnal, Modelling and simulations of the chemo–mechanical behaviour of leached cement-based materials: Leaching process and induced loss of stiffness, Cem. Concr. Res. 39 (2009) 763–772, https://doi.org/10.1016/j.cemconres.2009.05.010.

[63] L.B. Wang, L.A. Myers, L.N. Mohammad, Y.R. Fu, Micromechanics study on top-down cracking, Transp. Res. Rec. 2003 (1853) 121–133, https://doi.org/10.3141/1853-14.

[64] S.I. Kundalwal, S. Kumar, Multiscale modeling of stress transfer in continuous microscale fiber reinforced composites with nano-engineered interphase, Mech. Mater. 102 (2016) 117–131, https://doi.org/10.1016/j.mechmat.2016.09.002.

[65] Y. Xi, K. Willam, D.M. Frangopol, Multiscale modeling of interactive diffusion processes in concrete, J. Eng. Mech. 126 (2000) 258–265, https://doi.org/10.1061/(ASCE)0733-9399(2000)126:3(258).

[66] R.E. Rudd, J.Q. Broughton, Concurrent coupling of length scales in solid state systems, Physica Status Solidi (b) 217 (2000) 251–291, https://doi.org/10.1002/(SICI)1521-3951(200001)217:1<251::AID-PSSB251>3.0.CO;2-A.

[67] B. Mortazavi, E.V. Podryabinkin, S. Roche, T. Rabczuk, X. Zhuang, A.V. Shapeev, Machine-learning interatomic potentials enable first-principles multiscale modeling of lattice thermal conductivity in graphene/borophene heterostructures, Mater. Horiz. 7 (2020) 2359–2367, https://doi.org/10.1039/D0MH00787K.

[68] V. Yamakov, J.D. Hochhalter, W.P. Leser, J.E. Warner, J.A. Newman, G.P. Purja Pun, Y. Mishin, Multiscale modeling of sensory properties of Co–Ni–Al shape memory particles embedded in an Al metal matrix, J. Mater. Sci. 51 (2016) 1204–1216, https://doi.org/10.1007/s10853-015-9153-3.

[69] S. Nayak, S. Das, Strain sensing efficiency of hierarchical nano-engineered smart twill-weave composites: Evaluations using multiscale numerical simulations, Compos. Struct. 255 (2021), https://doi.org/10.1016/j.compstruct.2020.112905 112905.

[70] M.A.S. Matos, V.L. Tagarielli, P.M. Baiz-Villafranca, S.T. Pinho, Predictions of the electro-mechanical response of conductive CNT-polymer composites, J. Mech. Phys. Solids 114 (2018) 84–96, https://doi.org/10.1016/j.jmps.2018.02.014.

[71] M. Greminger, G. Haghiashtiani, Multiscale modeling of PVDF matrix carbon fiber composites, Modelling Simul. Mater. Sci. Eng. 25 (2017), https://doi.org/10.1088/1361-651X/aa6a8a 045007.

[72] Z. Chen, J. Huo, L. Hao, J. Zhou, Multiscale modeling and simulations of responsive polymers, Curr. Opin. Chem. Eng. 23 (2019) 21–33, https://doi.org/10.1016/j.coche.2019.02.004.

[73] H.B. Demuth, M.H. Beale, O. De Jess, M.T. Hagan, Neural Network Design, 2nd ed., Martin Hagan, Stillwater, OK, USA, 2014.

[74] K.L. Scrivener, A.K. Crumbie, P. Laugesen, The interfacial transition zone (ITZ) between cement paste and aggregate in concrete, Interface Sci. 12 (2004) 411–421, https://doi.org/10.1023/B:INTS.0000042339.92990.4c.

[75] M.A.S. Matos, S.T. Pinho, V.L. Tagarielli, Predictions of the electrical conductivity of composites of polymers and carbon nanotubes by an artificial neural network, Scr. Mater. 166 (2019) 117–121, https://doi.org/10.1016/j.scriptamat.2019.03.003.
[76] M.A.S. Matos, S.T. Pinho, V.L. Tagarielli, Application of machine learning to predict the multiaxial strain-sensing response of CNT-polymer composites, Carbon 146 (2019) 265–275, https://doi.org/10.1016/j.carbon.2019.02.001.
[77] B.D. Lubachevsky, F.H. Stillinger, Geometric properties of random disk packings, J. Stat. Phys. 60 (1990) 561–583, https://doi.org/10.1007/BF01025983.
[78] B.D. Lubachevsky, F.H. Stillinger, E.N. Pinson, Disks vs. spheres: Contrasting properties of random packings, J. Stat. Phys. 64 (1991) 501–524, https://doi.org/10.1007/BF01048304.
[79] Z. Ullah, Ł. Kaczmarczyk, S.A. Grammatikos, M.C. Evernden, C.J. Pearce, Multi-scale computational homogenisation to predict the long-term durability of composite structures, Comput. Struct. 181 (2017) 21–31, https://doi.org/10.1016/j.compstruc.2016.11.002.
[80] S. Nayak, N.M.A. Krishnan, S. Das, Microstructure-guided numerical simulation to evaluate the influence of phase change materials (PCMs) on the freeze-thaw response of concrete pavements, Constr. Build. Mater. 201 (2019) 246–256, https://doi.org/10.1016/j.conbuildmat.2018.12.199.
[81] P. Yang, S. Chowdhury, N. Neithalath, Strain sensing ability of metallic particulate reinforced cementitious composites: Experiments and microstructure-guided finite element modeling, Cem. Concr. Compos. 90 (2018) 225–234, https://doi.org/10.1016/j.cemconcomp.2018.04.004.
[82] M. Smith, ABAQUS/Standard User's Manual, Version 6.9, Dassault Systèmes Simulia Corp, United States, 2009.
[83] S. Das, A. Maroli, N. Neithalath, Finite element-based micromechanical modeling of the influence of phase properties on the elastic response of cementitious mortars, Constr. Build. Mater. 127 (2016) 153–166, https://doi.org/10.1016/j.conbuildmat.2016.09.153.
[84] T. Wu, P. Wriggers, Multiscale diffusion–thermal–mechanical cohesive zone model for concrete, Comput Mech. 55 (2015) 999–1016, https://doi.org/10.1007/s00466-015-1149-y.
[85] J. Roesler, G.H. Paulino, K. Park, C. Gaedicke, Concrete fracture prediction using bilinear softening, Cem. Concr. Compos. 29 (2007) 300–312, https://doi.org/10.1016/j.cemconcomp.2006.12.002.
[86] S. Nayak, N.M.A. Krishnan, S. Das, Fracture response of metallic particulate-reinforced cementitious composites: Insights from experiments and multiscale numerical simulations, Cem. Concr. Compos. 97 (2019) 154–165, https://doi.org/10.1016/j.cemconcomp.2018.12.026.
[87] S. Doner, S. Nayak, K. Senol, A. Shukla, N.M.A. Krishnan, I.K. Yilmazcoban, S. Das, Dynamic compressive behavior of metallic particulate-reinforced cementitious composites: SHPB experiments and numerical simulations, Constr. Build. Mater. 227 (2019), https://doi.org/10.1016/j.conbuildmat.2019.08.049 116668.
[88] M. Elices, C. Rocco, C. Roselló, Cohesive crack modelling of a simple concrete: Experimental and numerical results, Eng. Fract. Mech. 76 (2009) 1398–1410, https://doi.org/10.1016/j.engfracmech.2008.04.010.
[89] I. Goodfellow, Y. Bengio, A. Courville, Deep Learning, The MIT Press, Cambridge, Massachusetts, 2016.
[90] A. Kratsios, Characterizing the Universal Approximation Property, ArXiv:1910.03344 [Cs, Math, Stat]. (2020). http://arxiv.org/abs/1910.03344 (accessed August 30, 2020).
[91] D.W. Abueidda, S. Koric, N.A. Sobh, H. Sehitoglu, Deep learning for plasticity and thermo-viscoplasticity, Int. J. Plast. 136 (2021), https://doi.org/10.1016/j.ijplas.2020.102852 102852.
[92] D.P. Kingma, J. Ba, Adam: A Method for Stochastic Optimization, ArXiv:1412.6980 [Cs]. (2017). http://arxiv.org/abs/1412.6980 (accessed May 10, 2021).
[93] G.C. Cawley, N.L.C. Talbot, On over-fitting in model selection and subsequent selection bias in performance evaluation, J. Mach. Learn. Res. 11 (2010) 2079–2107.
[94] G.A. Lyngdoh, H. Li, M. Zaki, N.M.A. Krishnan, S. Das, Elucidating the constitutive relationship of calcium–silicate–hydrate gel using high throughput reactive molecular simulations and machine learning, Sci. Rep. 10 (2020) 21336, https://doi.org/10.1038/s41598-020-78368-1.
[95] K. Yang, X. Xu, B. Yang, B. Cook, H. Ramos, N.M.A. Krishnan, M.M. Smedskjaer, C. Hoover, M. Bauchy, Predicting the young's modulus of silicate glasses using high-throughput molecular dynamics simulations and machine learning, Sci Rep. 9 (2019) 8739.
[96] M. Stone, Cross-validatory choice and assessment of statistical predictions, J. Royal Stat. Soc.: Ser. B (Methodol.) 36 (1974) 111–133. https://doi.org/10.1111/j.2517-6161.1974.tb00994.x.
[97] S.M. Lundberg, S.-I. Lee, A unified approach to interpreting model predictions, in: I. Guyon, U.V. Luxburg, S. Bengio, H. Wallach, R. Fergus, S. Vishwanathan, R. Garnett (Eds.), Advances in Neural Information Processing Systems 30, Curran Associates, Inc., 2017: pp. 4765–4774. http://papers.nips.cc/paper/7062-a-unified-approach-to-interpreting-model-predictions.pdf (accessed September 14, 2020).
[98] S. Cohen, E. Ruppin, G. Dror, Feature selection based on the Shapley value, in: Proceedings of the 19th International Joint Conference on Artificial Intelligence, Morgan Kaufmann Publishers Inc., San Francisco, CA, USA, 2005: pp. 665–670.
[99] C. Molnar, Interpretable Machine Learning, n.d. https://christophm.github.io/interpretable-ml-book/ (accessed September 15, 2020).
[100] Y. Shen, P. He, X. Zhuang, Fracture model for the prediction of the electrical percolation threshold in CNTs/Polymer composites, Front. Struct. Civ. Eng. 12 (2018) 125–136, https://doi.org/10.1007/s11709-017-0396-8.
[101] B.M. Lee, K.J. Loh, A 2D percolation-based model for characterizing the piezoresistivity of carbon nanotube-based films, J Mater Sci. 50 (2015) 2973–2983, https://doi.org/10.1007/s10853-015-8862-y.
[102] W. Song, V. Krishnaswamy, R.V. Pucha, Computational homogenization in RVE models with material periodic conditions for CNT polymer composites, Compos. Struct. 137 (2016) 9–17, https://doi.org/10.1016/j.compstruct.2015.11.013.
[103] G. Yin, N. Hu, Y. Karube, Y. Liu, Y. Li, H. Fukunaga, A carbon nanotube/polymer strain sensor with linear and anti-symmetric piezoresistivity, J. Compos. Mater. 45 (2011) 1315–1323, https://doi.org/10.1177/0021998310393296.
[104] J.G. Gonzalez, S. Gupta, K.J. Loh, Multifunctional cement composites enhanced with carbon nanotube thin film interfaces, Proc. IEEE 104 (2016) 1547–1560, https://doi.org/10.1109/JPROC.2015.2503299.
[105] B.M. Lee, K.J. Loh, Carbon nanotube thin film strain sensors: comparison between experimental tests and numerical simulations, Nanotechnology 28 (2017), https://doi.org/10.1088/1361-6528/aa6382 155502.
[106] P. Xie, P. Gu, J.J. Beaudoin, Electrical percolation phenomena in cement composites containing conductive fibres, J. Mater. Sci. 31 (1996) 4093–4097, https://doi.org/10.1007/BF00352673.
[107] M. Abadi, P. Barham, J. Chen, Z. Chen, A. Davis, J. Dean, M. Devin, S. Ghemawat, G. Irving, M. Isard, M. Kudlur, J. Levenberg, R. Monga, S. Moore, D. G. Murray, B. Steiner, P. Tucker, V. Vasudevan, P. Warden, M. Wicke, Y. Yu, X. Zheng, TensorFlow: A System for Large-Scale Machine Learning, in: 2016: pp. 265–283. https://www.usenix.org/conference/osdi16/technical-sessions/presentation/abadi (accessed September 24, 2020).